Comparison between polar regions of Mars from HEND/Odyssey data

M.L. Litvak [a,*], I.G. Mitrofanov [a], A.S. Kozyrev [a], A.B. Sanin [a], V.I. Tretyakov [a], W.V. Boynton [b], N.J. Kelly [b], D. Hamara [b], C. Shinohara [b], R.S. Saunders [c]

[a] *Space Research Institute, Profsojuznaya street 84/32, Moscow 117997, Russia*
[b] *Lunar and Planetary Laboratory, University of Arizona, Tucson, AZ 85721, USA*
[c] *NASA Headquarters, Washington, DC 20546-0001, USA*

Abstract

In this paper, we have analyzed neutron spectroscopy data gathered by the High Energy Neutron Detector (HEND) instrument onboard Mars Odyssey for comparison of polar regions. It is known that observation of the neutron albedo of Mars provides important information about the distribution of water–ice in subsurface layers and about peculiarities of the CO_2 seasonal cycle. It was found that there are large water-rich permafrost areas with contents of up to ~50% water by mass fraction at both the north and south Mars polar regions. The water–ice layers at high northern latitudes are placed close to the surface, but in the south they are covered by a dry and relatively thick (10–20 cm) layer of soil. Analysis of temporal variations of neutron flux between summer and winter seasons allowed the estimation of the masses of the CO_2 deposits which seasonally condense at the polar regions. The total mass of the southern seasonal deposition was estimated as 6.3×10^{15} kg, which is larger than the total mass of the seasonal deposition at the north by 40–50%. These results are in good agreement with predictions from the NASA Ames Research Center General Circulation Model (GCM). But, the dynamics of the condensation and sublimation processes are not quite as consistent with these models: the peak accumulation of the condensed mass of CO_2 occurred 10–15 degrees of L_s later than is predicted by the GCM.
© 2005 Elsevier Inc. All rights reserved.

Keywords: Mars, surface; Mars, atmosphere; Mars, climate; Ices

1. Introduction

Two years of neutron mapping measurements onboard the Mars Odyssey spacecraft are presented based on High Energy Neutron Detector (HEND) observations. The HEND instrument is a part of the GRS suite, which is responsible for detection of epithermal and high energy neutrons produced within 1–2 m (for soils having very low hydrogen content) of Mars' subsurface (Mitrofanov et al., 2002, 2003a, 2003b). The neutron albedo and gamma-ray radiation of Mars are a result of the bombardment of the martian surface by the nuclei of primary galactic cosmic rays freely penetrating through the thin martian atmosphere (Masarik and Reedy, 1996). The leakage flux of neutrons strongly depends on the presence of hydrogen atoms. Subsurface water of even a few percent by weight significantly depresses the flux of epithermal and fast neutrons (Drake et al., 1988; Feldman et al., 1993). Therefore, neutron spectroscopy from the low altitude polar orbit is a highly sensitive method for measuring the global distribution of subsurface water on the planet.

There is a direct correspondence between the energy of a detected neutron and the most probable depth at which it was produced. The production rate of fast neutrons has a maximum at depths of less than tens of centimeters, while the epithermal neutrons mainly originate 1–2 m below the surface of dry soil. Combining the HEND measurements of neutrons in different energy ranges from 0.4 eV to 15 MeV and higher, one may reconstruct the water abundance distribution, starting from the top, down to ~1 m of depth. These data allow the testing of various models that describe the layered structure of the soil in the shallow subsurface.

Neutron and gamma-ray measurements onboard Mars Odyssey have discovered large regions with a huge amount of water–

---

ice in the shallow subsurface placed poleward of 60 degrees at the north and south poles (Boynton et al., 2002; Feldman et al., 2002; Mitrofanov et al., 2002, 2003a, 2003b, 2004a, 2004b). These areas may be called northern and southern permafrost regions, because water–ice is stable over the entire martian year at these latitudes (Mellon and Jakosky, 1995; Mellon et al., 2003, 2004). It was also found that subsurface water–ice has a layered structure at southern regions. It was suggested that the bottom layer, containing on average 35–100% water–ice by weight, is covered by a relatively dry layer of varying thickness (Boynton et al., 2002; Tokar et al., 2002; Prettyman et al., 2004). Determining the amount of water–ice accumulated at the polar regions, and how deep it is placed below the surface, plays an important role in the understanding of past and current changes of the climate on Mars. Moreover, it may give rise to speculations concerning the search for traces of life.

Another phenomenon, which may be studied by nuclear methods, is global seasonal redistribution of atmospheric CO_2 between snow depositions at the poles. Seasonal changes at the martian poles are a very significant feature of the martian climate. This atmospheric redistribution involves more than 25% of the total atmospheric mass (Forget and Pollack, 1996). The spatial and temporal properties of this process are mainly controlled by solar insolation (Leighton and Murray, 1966). The study of CO_2 and H_2O cycles is a high priority of martian climatology and may give us a more detailed understanding of the current and past climate on Mars.

During the previous martian year, we have observed the cyclic process of the accumulation of CO_2 frost during fall and winter when the temperature falls below the CO_2 condensation point. During the spring and summer, the CO_2 deposit sublimates back into the atmosphere, revealing the residual polar caps. While the northern residual cap is thought to consist of pure water–ice, in the southern region, the CO_2 deposit does not completely sublimate during summer. The residual cap on the south pole is covered by a CO_2 frost even during the southern summer (Kieffer, 1979; Tokar et al., 2003). The annual balance of CO_2 deposition and sublimation is the important parameter determining the climate of Mars. The knowledge of the behavior of this cycle in the past epochs is a means to build a model of climate changes on the planet. The thickness of CO_2 snow in the winter above ±60 degrees of latitude varies from tens of centimeters up to ∼1 m (Smith et al., 2001). Taking into account that the neutron production layer is about 1–2 m thick, one may expect significant temporal variations of neutron albedo for the northern and southern permafrost regions throughout the martian seasons. During the summer, the flux and energy spectrum of the neutron albedo is determined by the production and moderation of neutrons inside a water–ice-rich layer of the subsurface. (The presence of hydrogen is the main reason for strong moderation, because the H proton in the water molecule gets about half of the energy at each collision with a neutron.) In contrast, during the winter, when the thickness of the CO_2 deposit approaches its maximum, the layer of neutron production shifts from the regolith to the layer of overlying carbon dioxide, which contains a small amount of water and where

the moderation of neutrons is not so efficient. If the thickness of the CO_2 layer is large enough, about 1 m or so, all of the escaping neutrons are produced in the CO_2 frost, and a further increase in the thickness of the CO_2 does not change the leakage flux of neutrons.

So, in summer, when the CO_2 deposit sublimes from the surface, the flux of epithermal and high energy neutrons from the poleward permafrost regions goes down. On the other hand, the flux increases during winter due to the deposition of atmospheric CO_2 onto the surface.

Measurements of neutron flux onboard Mars Odyssey by the HEND and the Neutron Spectrometer clearly display significant variations of neutron flux between the summer and winter seasons of a given year (Mitrofanov et al., 2003a; Feldman et al., 2003a; Litvak et al., 2003a, 2003b, 2004). The flux of epithermal neutrons above the permafrost regions varies between winter and summer seasons by a factor of several. The amplitude of the variations is larger at higher polar latitudes. At the border of the seasonal cap (minimal thickness of the CO_2 deposit), the increase is quite small (1.1–1.3 times), but at more poleward latitudes (>80 N/80 S), the change in neutron flux corresponds to a factor of 2–3 (Litvak et al., 2003a, 2003b).

In this paper, we compare properties of northern and southern permafrost regions using the data from neutron measurements by HEND onboard Odyssey. The global neutron mapping of Mars' surface started in February 2002 at the end of southern summer and is in progress now. It provides the unique opportunity to study the entire martian year of seasonal changes of Mars at high latitudes. Using these data, the comparative analysis between south and north poleward regions may be done in two ways. According to the first method, we will compare CO_2 frost-free ground soil surfaces to understand the major differences between the water–ice distributions. The second way uses the comparison of the time profiles of condensation and sublimation of seasonal carbon dioxide deposits at different regions together with the estimation of their total masses.

2. Instrumentation and condition of orbital mapping

HEND consists of four detectors to provide measurements of neutrons within the broad energy range from 0.4 eV up to 15 MeV (Boynton et al., 2004). It has three [3]He proportional neutron counters coated by a Cd shield and placed inside moderating polyethylene enclosures with different thicknesses. These counters record thermal neutrons by neutron capture reactions. When neutrons come into the detector volume, they lose energy in the polyethylene moderator and are brought down to thermal energies. They are then detected by the proportional counters. The moderation efficiency in polyethylene depends on its thickness. The Large Detector (LD) with the thickest moderator (∼30 mm) is the most sensitive to neutrons with energies 10 eV–1 MeV. The Medium Detector (MD) with a 14-mm-thick moderator is used for detection of neutrons in the energy range 10 eV–100 keV. The Small detector (SD) with the thinnest (3 mm) moderator is sensitive to neutrons with energies from the cadmium threshold 0.4 eV up to 1 keV. The combination of data from all three detectors (SD, MD, and LD)

provides information about the spectral density of the neutrons in the broad energy range from 0.4 eV to 1 MeV.

The organic stylbene scintillator (SC/IN) is used to detect neutrons with energies higher than 1 MeV. This scintillator detects high-energy neutrons by recording flashes of light from recoil protons knocked out of the organic crystal lattice by neutrons. In space, this organic scintillator may also detect the primary protons of cosmic rays. In addition, cosmic-ray electrons and secondary electrons produced by gamma-ray photons are also well detected in the crystal. There is a special electronic board in the instrument, which separates counts of protons from counts of electrons by pulse shape analysis. This technique provides quite good quality of separation between protons and electrons. The highest probability of making the mistake of detecting an electron signal as a proton signal in such separations is about 10^{-3}, which corresponds to the lowest amplitude counts in the entire energy range. To reject the primary protons of cosmic rays, HEND uses the active anticoincidence shield of CsI around the stylbene detector. It shields the organic scintillator from the open sky except in the direction of the martian surface.

The Mars Odyssey spacecraft is a relatively massive body which produces secondary nuclear radiation under bombardment by the galactic cosmic-ray flux. Orbital neutron measurements made by the HEND instrument aboard Odyssey contain a contribution from the spacecraft, called the spacecraft background. The spacecraft background was determined by measuring the number of neutron counts recorded during nominal collection intervals in the HEND detectors during the cruise and aerobraking phases of the mission when the spacecraft was far from both Earth and Mars. The average number of counts per collection interval in each neutron signal is taken as the isotropic galactic cosmic-ray flux induced spacecraft background. The isotropic galactic cosmic-ray flux induced background is only an approximation of the spacecraft background. When the spacecraft is in an orbit close to Mars, the planet partially shields the spacecraft from the galactic cosmic-ray flux. The partial shielding decreases the number of galactic cosmic-rays hitting the spacecraft, therefore decreasing the secondary nuclear radiation produced and causing a decrease in the spacecraft background counts. This decrease in background counts per measurement interval is taken into account by multiplying the isotropic galactic cosmic-ray flux induced background by $(1 - \Omega(t)/4\pi)$, where $\Omega(t)$ is the solid angle subtended by Mars from the current point in the spacecraft orbit. The equation used to estimate the background subtracted signal S_i for each HEND detector in the ith measurement interval is:

$$S_i = C_i - B_i \cdot \frac{4\pi - 2\pi \cdot (1 - \cos\theta_i)}{4\pi}, \tag{1}$$

where C_i—measured counts during ith collection interval in given detector in given set of energy channels, B_i—counts from isotropic galactic cosmic rays in ith collection interval in given detector in given set of energy channels (measured far away from Mars during cruise and aerobraking mission phases), θ_i—angular radius of Mars as seen from Odyssey during ith collection interval, S_i—background subtracted signal in ith collection

interval calculated for given detector in given set of energy channels.

The galactic cosmic-ray flux induced spacecraft background is removed from every measurement interval, resulting in a time-series of background subtracted measurements of each of the HEND neutron signals.

There is also another source of background affecting the HEND detector. This background is due to neutrons backscattered from the spacecraft. The data gathered during the aerobraking phase of the mission shows that this background component is several times lower then the primary background presented in Eq. (1). This backscattered background component is proportional to neutron flux from Mars, i.e. it is proportional to S_i. One may take this component into account as an additional part of the efficiency function, which describes the transformation of the incoming flux of neutrons into counts in the detectors. However, we use the normalization procedure described below, where all signals (S_i) from neutrons at different measurement intervals (i) are normalized by the maximum signal from Solis Planum. To first order, we believe that this normalization procedure excludes the backscattering effect from our analysis. Once the time-series background subtracted data have been produced for each of the five HEND signals, the data is examined to determine if data collection occurred during a solar particle event. Solar particle events (SPEs) significantly influence the HEND detectors' counting rates, often increasing the counting rates by several orders of magnitude. Any data collected during times of intense solar activity are flagged and excluded from further routine data processing, as the goal of the routine data processing is to create a data set that allows examination of the temporal and spatial changes in martian neutron albedo over time. The exclusion of data collected during SPEs is based on visual inspection of the data combined with information from Earth observation of solar activity (i.e. GOES spacecrafts). The visual inspections and comparisons with other data sets do not guarantee that every collection interval that has been influenced by heightened solar activity has been excluded. It is possible that weak traces of SPEs may remain in the data.

The time of a single measurement is ~20 s. During this time, the spacecraft travels about 1 degree of arc over the planet. The spatial resolution for neutron measurements is affected by the presence of the martian atmosphere. The results of numerical simulations show that at certain points in the orbit the instrument collects neutrons from as large a surface area as 600×600 km. In some directions, the HEND field of view is limited by the spacecraft body (~380 kg, primarily consisting of Al), which is important for the data deconvolution because the probability of the interaction of neutrons with the spacecraft body can be quite large. This also means that the HEND footprint area is not circular. It is smaller than 600×600 km and is offset from the nadir direction. However, the offset effect is negligible for the regions selected for this study, which is proven by directly comparing data for each surface element as measured during both North-to-South and South-to-North flight conditions, when either the southern or the northern parts of the HEND field of view are partially screened by the spacecraft.

Another possible source of systematic error involves spatial mixing as it was introduced by Tokar et al. (2002) and Prettyman et al. (2004). The GRS, HEND, and NS have similar spatial response characteristics and spatially mix the data in comparable ways. For example, there is a transition region between high and mid southern latitudes in which the GRS, HEND, and NS sample both the polar water rich region and the dry low latitude region. This gives rise to a broad, smoothly varying profile for the interpreted water abundance between low and high latitudes when spatial mixing is ignored, as was demonstrated by Tokar et al. and Prettyman et al. as mentioned above. These studies showed that the NS data were generally consistent with an abrupt boundary between the ice-rich polar region and the relatively dry mid-latitudes when spatial mixing was included in models of the counting data. Spatial mixing was also shown to result in a systematic bias in the amount of water in the ice table, giving a lower bound on this quantity. Because we believe that this effect does not significantly bias averaged estimations of minimal water abundances in the selected regions, we did not account for this effect in our data analysis in the same manner as was done in Tokar et al. (2002) and Prettyman et al. (2004).

Taking spatial resolution into account, we limited our data processing by the analysis of relative large regions only. For the northern hemisphere, we selected 74 partially intersecting regions covering the surface area from 60 °N up to the North Pole. The regions selected along the boundary of the northern ice-rich area (∼60 °N) are 15° (longitude) by 10° (latitude). The regions at the pole have sizes equal to 72° × 10°. The southern seasonal cap was covered by a grid of 98 regions starting from 50 °S. Like in the northern case, the southern border regions are 15° × 10°, and the southern near-polar regions are 72° × 10° (longitude × latitude).

3. Model dependent deconvolution of HEND neutron data

The measurements of the subsurface structure of Mars are based on the comparison between the orbital observation data and predictions of numerical models of neutron leakage flux from the surface. To make this comparison, one needs to define the model of the neutron production layer. The simplest version of this model has to contain 3 or 4 layers: the top layer is the martian atmosphere, the middle layer represents the variable deposition of carbon dioxide on the surface, and the bottom layer (or two layers) correspond(s) to the structure of the subsurface soil. Each layer is comprised of a different substance with a different composition of elements, and each layer has unique properties for producing and moderating neutrons that escape from the martian subsurface up to the spacecraft.

The martian atmosphere has variable thickness at different points on Mars, and it also varies with the seasons of the martian year. It is known that the presence of the thin martian atmosphere influences orbital neutron fluxes as a function of their energy (see, e.g., Prettyman et al., 2003). To take these effects into account, the layers of martian atmosphere were included in the numerical modeling. The composition of the atmosphere was fixed as the following: carbon dioxide (CO_2)—95.32%; nitrogen (N_2)—2.7%; argon (Ar)—1.6%; oxygen (O_2)—0.13%; carbon monoxide (CO)—0.08%. The atmospheric column density was taken from the Ames GCM predictions for given regions and seasons (Haberle et al., 1993).

The layer of the CO_2 deposit can be described by only one free parameter, which can be used to calculate column density of the deposition. Using the best fitting value of this parameter, one may estimate the column density of the carbon dioxide deposition for different periods of time and for different surface elements of the planet. The creation of a multidimensional model of CO_2 deposition (thickness vs time and position on the martian surface) is one of the main goals of this study. With the exception of the south polar residual cap, this layer disappears during the summer and has the largest thickness at the end of the winter for each hemisphere.

The last layer (or layers) in our model describe(s) the structure of the shallow subsurface. To study the structure of the regolith, one may use summer observations only, when the layer of neutron production does not contain the layer of seasonal CO_2 deposition. We may define this study as *Task1* for determining the structure of the ground soil. When this *Task1* is completed and the structure of the ground soil is known, one may use observational data for fall–winter–spring seasons to determine the variable thickness of the layer of CO_2 deposition. This *Task2* will provide the multidimensional model of this deposition.

For simplicity in *Task1*, we start by assuming that the ground soil has a homogeneous composition throughout its depth. According to this assumption, the water content in the soil is described by a single parameter: the water mass fraction, ζ_{hom}. The composition of the dry soil fraction $(1 - \zeta_{hom})$ was taken from the APXS/Pathfinder observations (Wanke et al., 2001; Foley et al., 2003a, 2003b). *Task1* in this case is associated with searching for the best fitting value of the single free parameter, ζ_{hom}, for the summer-time data gathered in HEND observations.

If the model with depth-homogeneous soil is not supported by the observational data (see below), the next level of complexity corresponds to adding an additional layer to the structure of the soil. By weight, the top layer is composed of 2% water and 98% soil with the composition found by APXS/Pathfinder (Wanke et al., 2001; Foley et al., 2003a, 2003b). The first value reflects the minimal amount of bound water which may be found in the upper layers of the martian subsurface (see, for example, Foley et al., 2003b; Prettyman et al., 2004). The thickness of the upper layer, h_{up}, is used as the first free parameter of the shallow subsurface. Water content, ζ_{down}, is the second free parameter of the subsurface structure. The bottom layer consists of ζ_{down} water wt% and $(1 - \zeta_{down})$ soil wt% with APXS/Pathfinder composition. In this case, *Task1* is completed when the best fitting values for both parameters, $h_{up}^{(min)}$ and $\zeta_{down}^{(min)}$, are found for each surface element according to the data accumulated during summer-time observations.

Besides selecting a numerical model to deconvolve water abundance in the martian subsurface from relative changes of neutron flux through the planet's surface, one ought to apply a normalization to an absolute value of water content in a particu-

lar region of Mars. The best candidate for such a reference area may be founded at equatorial latitudes (Solis Planum) where neutron flux approaches its maximum value. It is the driest region of Mars, and it is an area that is not affected by seasonal CO_2 precipitation. This normalization allows us to exclude the systematic errors caused by effects of temporal variations of neutron emission of Mars due to the variable flux of charged particles from the Sun, variations of Galactic Cosmic Ray flux, temperature drifts and possible degradation of the gain in the HEND detectors. An additional analysis has also shown that temperature drifts (the HEND electronics and detectors are kept in the temperature range 0–5 °C) and degradation of gain (comparative analysis for different periods of the mission has confirmed excellent stability of spectra shapes) are negligible.

For the analysis discussed in this paper, we have fixed the minimal content of water in the martian surface (Solis Planum) at the 2% level. This choice is supported by the "ground truth" (APXS measurements of bound water, see Foley et al., 2003b), numerical simulations based on "winter" normalization, estimation of minimal abundance of water (Prettyman et al., 2004) and comparisons between HEND, NS and GRS data.

The winter normalization procedure was initially suggested by Feldman et al., 2003a, 2003b. Following this approach, we have selected and modeled HEND data gathered poleward of 85 °N during north polar winter ($L_s = [0°, 20°]$). For these measurements, we have used a two-layer model (soil + CO_2 frost) of the martian subsurface. In this model, the bottom semi-infinite layer simulated the basement terrain composed of 100% H_2O and was covered by 65 g/cm^2 of CO_2 frost (see, for example, Feldman et al., 2003a, 2003b, 2004). Using such a normalization to winter north polar data, we are able to estimate the content of water in other regions of Mars. For Solis Planum, such an estimation resulted in $2.1 \pm 0.1\%$ water provided this region is fitted by a homogeneous model with APXS composition and an unknown content of water.

A minimum abundance of water in the martian subsurface of around 2% by weight is also supported by the analysis of Prettyman et al. (2004), based on the saturation of fast neutrons gathered by the NS instrument.

Finally, we have also found that estimations of the minimum water abundance at equatorial regions from neutron and gamma data (presentations of I. Mitrofanov/HEND, W. Feldman/NS and W. Boynton/GRS at 6th International conference on Mars, Pasadena, 2003, see also Feldman et al., 2003b, 2004) gives approximately the same values for Solis Planum.

When the solution to *Task1* is found for a selected surface element of Mars, the best fitting parameters of *Task1* can be fixed, and the search for the solution to *Task2* is started with only one free parameter: the column density, ξ_{CD}, of carbon dioxide deposition.

The search for appropriate solutions to *Task1* and *Task2* is based on the minimization procedure of the difference between the set of observed counts in the HEND sensors (SD, MD, LD, SC/IN) and the set of model-predicted counts, which correspond to testing the model with the given parameter(s). The minimization function can be presented as the following ex-
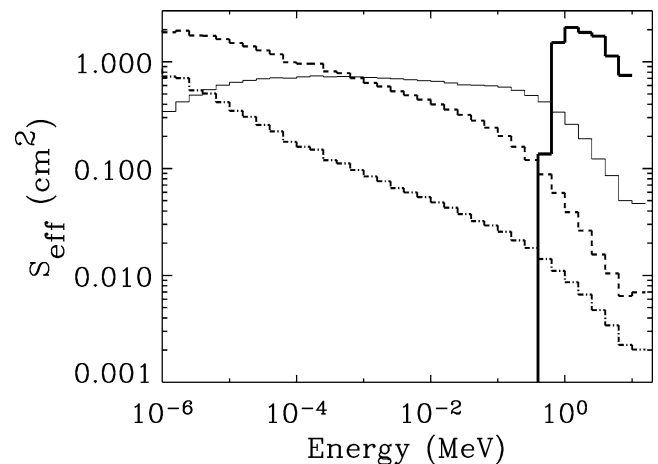

Fig. 1. Efficiency functions for the HEND detectors. The thick line corresponds to the efficiency of the inner scintillator stylbene detector. The thin, dash and dash–dot lines correspond to the LD, MD, and SD detectors, respectively.

pression:

$$S(P_j) = \sum_i \left(\frac{S_i - M_i(P_j)}{\sigma_i} \right)^2, \tag{2}$$

where S_i are background subtracted counts from the HEND sensors ($i = 1, 2, \ldots, k$), M_i are model predicted counts according to numerical simulations for selected model parameters P_j, and σ_i is the total error including statistical and calculation errors (MCNPX errors + uncertainty of response functions, see below).

The M_i value may be calculated from following equation:

$$M_i = \int_{E_1}^{E_2} \frac{dN}{dE}(E) \cdot \mathrm{Seff}_i(E)\, dE, \tag{3}$$

where dN/dE is the neutron leakage spectrum of the orbit simulated by MCNPX code for the selected martian model with the given atmosphere, regolith structure and thickness of CO_2 frost (see, for example, Prettyman et al., 2004, Appendix B). The irradiation of the martian surface is deduced from the known spectral density of CGR flux (see, for example, Reedy, 1987).

$\mathrm{Seff}_i(E)$ is the detector efficiency function (see Fig. 1). These response functions were generated from ground calibrations for each HEND detector as it was packaged in the flight version of HEND. (The HEND is a small instrument and separate detectors may influence each other.) To avoid possible misleading interpretations due to systematic errors, we fixed the maximal errors (~10% as estimated during ground calibrations of HEND data) of the response functions and have taken them into account in the minimization procedure (2). E_1 and E_2 define the selected energy interval E.

In numerical simulations, we also took into account the angular dependency of the response functions for each HEND detector as it was packaged in HEND flight version. For the HEND, as a stand alone instrument, calibrations have shown that the angular dependency of the efficiency functions is not the dominating factor when compared to the energy dependency. The difference between arbitrary functions $\mathrm{Seff}(E, \alpha1)$
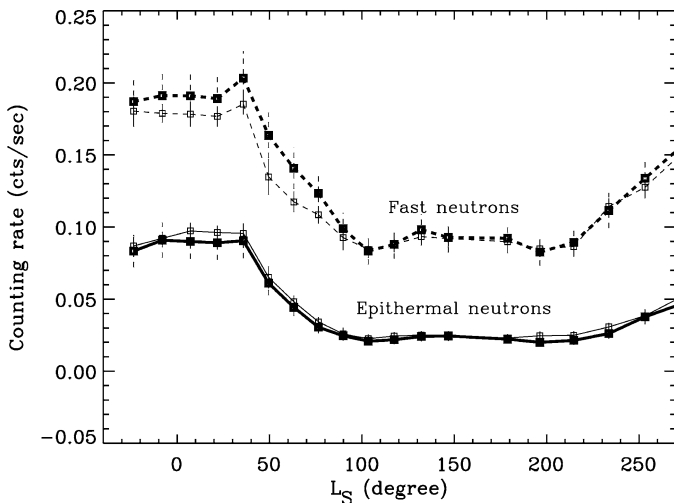
Fig. 2. The illustration of the direct comparison between real HEND counting rates (thick line) and best fit model predictions (thin line).

and $Seff(E, \alpha 2)$ calculated for a given HEND detector can be fitted by a normalization constant and is diminished if in data processing we normalize to the counts registered above a particular region. Onboard Odyssey, the HEND instrument is partially screened from martian neutron flux by the mass of the spacecraft. For example, for the fast neutrons with energies of about 1 MeV, the probability of no interaction may be roughly estimated as 0.08, showing that most 1 MeV neutrons traveling through the spacecraft are attenuated. But the comparison between maps (counting rates in HEND epithermal and fast neutron detectors) created for North-to-South and South-to-North flybys have shown that for the regions selected for the analysis the effect of partial screening is non-significant.

Due to unavailable information about the spacecraft model, we did not take into account in our data analysis the backscattering of martian neutrons in the spacecraft body. To solve this problem, we consider the spacecraft as a black body and use normalization to Solis Planum. We believe that this method in data reduction suppresses the problems with HEND's obstructed field of view to the first order of magnitude.

The quality of minimization may be estimated using a χ_n^2 distribution with n degrees of freedom, where $n = k - p$ (k is the number of independent signals, and p is the number of free parameters in the tested model). Usually, the tested hypothesis can be accepted if the probability to get the minimal value, $S_{min}(P_j)$, due to random fluctuations of χ_{k-p}^2 is larger than 0.01–0.05. If the probability lies below the acceptance level, one should conclude that the difference between model predictions and observed counts is not a result of random fluctuations, and the model is not supported by observations. The total number, k, of independent signals varies depending on the model.

The correspondence between real HEND data and best fit model predictions is illustrated by Fig. 2 where epithermal and fast neutron counting rates are compared with model estimations.

4. Distribution of water–ice at the Mars polar regions

We have solved *Task1* to estimate the content of water in the subsurface for enormous permafrost territories surrounding the north and south poles. All numerical calculations were performed using the MCNPX Monte Carlo code (Waters, 1999), which transforms the flux of Galactic Cosmic Rays into the count rates in the detectors of HEND in orbit.

The sensitivity of the tested model to the structure of the regolith is determined by comparing the statistics at different energy bands. Fast neutrons are mainly produced at smaller depths than neutrons with lower energies (epithermal). Taking into account that the HEND detectors cover a relatively large energy range (0.4 eV–15 MeV), one may verify the layered structure of the martian subsurface by analyzing neutron fluxes that registered in different energy bands of the HEND instrument. This approach was realized through the minimization procedure (2) in which measurements of neutron fluxes at different detectors (different energy bands) are compared with model predictions. The selection between the homogeneous or double-layered models is based on the incompatibility of low energy (SD, MD, LD detectors) and high energy channels (Stylben detector) in the minimization sum (2). This occurs in the case that hydrogen is inhomogeneously distributed throughout the depth.

The martian atmosphere and the composition of the regolith (except hydrogen) play an important, but not dominant, role in forming orbital neutron leakage spectra. The major effect is defined by the distribution of hydrogen in subsurface layers of Mars.

The first step was to test the homogeneous model of the subsurface for both polar regions (see Table 1). For the latitude belts of the northern region, the homogeneous model works very well and gives very high acceptance probabilities. We believe that a more complex model of the subsurface is not necessary for the northern permafrost region. The estimated average content of water–ice corresponds to 44%, 25%, and 13% by weight for the northern polar region (>80°N), the northern high latitude belt (70°N–80°N), and the northern boundary belt (60°N–70°N), respectively. A similar analysis was repeated for the set of 74 regions (see Section 2) covering the northern permafrost territory. It was found that the homogeneous model of the subsurface also works well for this sample of separate regions as it does for the data averaged along the latitude belts.

Implementation of the homogeneous model for the southern water–ice-rich region has not been so successful (Table 1). In all cases tested, the minimum of the function (2) was found to be too large to have resulted from statistical uncertainty; the probabilities of acceptance for the homogeneous models did not exceed several percent. According to statistical rules, one has to reject the homogeneous model of the subsurface for the latitude belts of the southern water–ice-rich region. One possible explanation may be that strong regional variations of the water content exist within the southern region. According to this theory, the homogeneous model could not describe the entire latitude belt, but it would be acceptable for separate regions

Table 1
Homogeneous model of regolith: content of water in different latitude belts

Martian season, L_s	Coordinates	Water content (%)	Probability for homogeneous model
120°–150°	0°–360° >80°N	44.1	0.6
120°–150°	0°–360° 70°N–80°N	24.8	0.4
120°–150°	0°–360° 60°N–70°N	12.5	0.7
330°–360°	0°–360° >80°S	22.7	0.004
330°–360°	0°–360° 70°S–80°S	19.5	0.03
330°–360°	0°–360° 60°S–70°S	11.2	0.07

within it. We also tested this possibility for a set of 98 different surface elements (see Section 2), and again revealed the lack of correlation between the HEND experimental data and the numerical simulation. In most of these regions, the derived acceptance probabilities have been found to be below the acceptable level. In fact, the homogeneous model has been rejected as an appropriate description of the southern water–ice territory.

The next level of complexity of the subsurface model corresponds to the adding a double layer with free parameters: h_{up} and ζ_{down} (see section above). To increase the sensitivity of the model to the layered structure, five observational signals from the HEND detectors (SD, MD, LD, SC/IN for 0.85–2.5 MeV, and SC/IN for >2.5 MeV) were used when testing the minimization of function (2).

The average HEND data for the southern latitude belts support the double-layered model of the subsurface. The best fitting values of the free parameters correspond to a rather high acceptance probability (more than 30%). The average column density of the top dry layer is about 16–25 g/cm^2, and the average content of water–ice is about 55% by weight above 70°S and then decreases to 25% by weight at the southern boundary belt: 60°S–70°S. The south residual cap is covered by CO_2 frost all year round and should be treated separately. However, the neutron data show that the CO_2 coverage of the residual cap at the South does not dominate the data for selected regions within 80°–90° latitude during the summer season. Indeed, we measured a very large increase of the neutron albedo for this region during the winter season, when the seasonal layer of CO_2 covers the surface. For the summertime, we found that the double-layered model of the surface is acceptable to fit the data from the south polar region. (This result differs from that found by Tokar et al. (2003) and Prettyman et al. (2004).) Therefore, the residual cap with dry CO_2 ice at the top was not removed from the data.

The detailed analysis of a large set of experimental data gathered for both the northern (74 surface elements) and southern (98 surface elements) regions of Mars (see Tables 2 and 3) revealed that the main difference between these regions is not only the content of water–ice, but the structure of the subsurface (see also Mitrofanov et al., 2004a, 2004b). In the north, the data agrees with the depth-homogeneous model. It means that dirty water–ice may be found at surface level. On the contrary, in the south, the water–ice is covered by a dry top layer with a thickness >15 g/cm^2. Below the dry layer, the water–ice content is found to be quite similar to the content of water–ice in the North, except that the southern weight fraction of water is larger by 5–10% (see also Mitrofanov et al., 2004a, 2004b). Assuming a density of 1.6 g/cm^3 for this dry layer, the column density value may be converted to about 10–20 cm of dry blanket above the ice-rich soil at the southern permafrost territory.

Besides differences in the vertical structure and content of water, there is a sharp distinction in the spatial distribution of water–ice in the northern and southern hemispheres. In the south, the region with the maximum content of water–ice is significantly larger than in the north (see Fig. 3). In the northern hemisphere, the maximum content of ice is limited by the boundary of the north residual cap. In the southern hemisphere, maximum ice content is distributed over a much larger territory. One may say that it is roughly limited by latitudes poleward of 75°S.

For both northern and southern regions, the average content of water–ice exceeds about 50–60% by weight, which corresponds to a volume fraction of more than 60%, i.e. the ice is the main substance of the subsurface. Even in the boundary belts, the fraction of the ice by volume is still found to be very large: about 13% by weight in the north and 25% by weight in the south. The high fraction of water–ice is relevant to theories of Mars evolution (Mellon and Jakosky, 1995). One has to understand how the subsurface was formed with this enormous fractional volume of water–ice and was then preserved up to the current time. The ice content of the frost layer (more then 50% by volume) is too great to be deposited by vapor diffusion and condensation into pores (see also Tokar et al., 2003 and Prettyman et al., 2004). It means that ice must have been deposited by some other mechanism. The modern theories of water ice stability in the martian subsurface appeal to climate variations resulting from quasi-periodic variations in orbital parameters. Mars' obliquity defining solar insolation of the martian surface has ranged from 14° to 48° (Touma and Wisdom, 1993; Laskar et al., 1993, 2002). Climate models predict that during periods of high obliquity, ice stability zones are shifted to the equator, while for low obliquity periods, they shrink back toward the polar caps (Richardson et al., 2002, 2003; Haberle et al., 2003; Mischna et al., 2003). For example, with obliquity >45° (several Myr ago), it is predicted that water ice should be stable at the equator through the year (see, for example, Richardson and Wilson, 2002). During the past 300 kyr, the obliquity has oscillated around 25°. During this time, the water ice was stable only at polar zones (>60° latitudes) and was removed from mid-latitudes. Traces of the shrinking ice-rich mantle are found through geological surveys of regions laying between 30° and 60° latitude (Head et al., 2003).

It is interesting to compare ice depths found by the analysis of HEND data with maps of ice table depth based on subsurface ice stability models (Mellon, 2003). In the case of the northern territories (>60°N latitude), the ice stability model predicts ice

Table 2
Northern hemisphere—parameters of homogeneous model

North regions coordinates (degree)				Water (%)	Probability for homogeneous model
Longitude1	Longitude2	Latitude1	Latitude2		
0	15	60	70	14.4	0.4
15	30	60	70	12.5	0.3
30	45	60	70	12.9	0.9
45	60	60	70	10.5	0.7
60	75	60	70	10.9	0.3
75	90	60	70	11.8	0.0
90	105	60	70	11.7	0.3
105	120	60	70	14.1	0.1
120	135	60	70	15.7	0.1
135	150	60	70	14.3	0.2
150	165	60	70	15.6	0.1
165	180	60	70	14.1	0.5
180	195	60	70	15.5	0.2
195	210	60	70	24.6	0.3
210	225	60	70	21.9	0.3
225	240	60	70	27.4	0.7
240	255	60	70	25.7	0.8
255	270	60	70	22.2	0.3
270	285	60	70	12.6	0.2
285	300	60	70	8.6	0.1
300	315	60	70	7.2	0.5
315	330	60	70	7.6	0.4
330	345	60	70	9.1	0.1
345	360	60	70	12.7	0.4
0	18	65	75	18.8	0.4
18	36	65	75	18.4	0.3
36	54	65	75	17.6	0.4
54	72	65	75	15.7	0.2
72	90	65	75	15.7	0.0
90	108	65	75	18.3	0.2
108	126	65	75	19.1	0.4
126	144	65	75	24.0	0.1
144	162	65	75	18.4	0.6
162	180	65	75	21.8	0.1
180	198	65	75	24.2	0.4
198	216	65	75	24.9	0.3
216	234	65	75	30.6	0.6
234	252	65	75	30.5	0.5
252	270	65	75	27.0	0.3
270	288	65	75	16.8	0.2
288	306	65	75	10.1	0.2
306	324	65	75	8.4	0.2
324	342	65	75	10.9	0.1
342	360	65	75	15.7	0.3
0	24	70	80	25.9	0.6
24	48	70	80	27.3	0.1
48	72	70	80	28.2	0.1
72	96	70	80	19.1	0.1
96	120	70	80	26.1	0.2
120	144	70	80	24.6	0.3
144	168	70	80	28.0	0.3
168	192	70	80	27.3	0.1
192	216	70	80	25.0	0.2
216	240	70	80	31.1	0.6
240	264	70	80	27.6	0.4
264	288	70	80	19.9	0.2
288	312	70	80	15.6	0.2
312	336	70	80	13.8	0.2
336	360	70	80	21.9	0.1
0	36	75	85	33.8	0.4
36	72	75	85	30.1	0.5

Table 2 (*continued*)

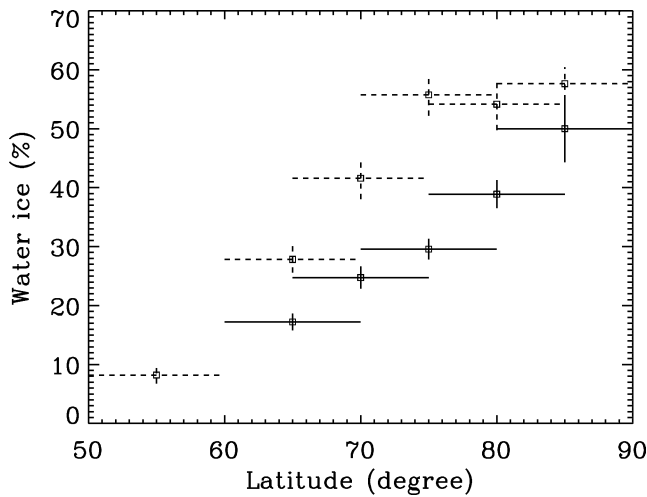| North regions coordinates (degree)				Water (%)	Probability for homogeneous model
Longitude1	Longitude2	Latitude1	Latitude2		
72	108	75	85	32.1	0.2
108	144	75	85	32.3	0.3
144	180	75	85	30.0	0.3
180	216	75	85	30.2	0.2
216	252	75	85	30.4	0.4
252	288	75	85	25.0	0.2
288	324	75	85	23.1	0.2
324	360	75	85	33.4	0.4
0	72	80	90	50.0	0.1
72	144	80	90	40.1	0.2
144	216	80	90	38.4	0.4
216	288	80	90	40.3	0.6
288	360	80	90	55.1	0.4

Fig. 3. Distribution of water–ice in the northern hemisphere (solid line) and southern hemisphere (dashed line).

Fig. 4. The depth of occurrence of the water bearing layer in the southern hemisphere.

depths ranges from several centimeters up to 20–30 cm, while analysis of HEND data claims that water ice is homogeneously distributed throughout depth and may be actually observed at surface level. For the southern hemisphere, HEND observations are more similar to the model predictions except at polar latitudes where the ice stability model predicts smaller water ice depths than were found in the analysis of neutron data.

Another work based on analysis of neutron data (NS/Mars Odyssey data, Prettyman et al., 2004) claims that the regolith in southern regions ($>60\,°S$) may be fitted by a double-layered model with 2% water (by weight) in the upper layer, $60 \pm 10\%$ water (by weight) in the bottom layer, and an upper layer column density of ~15 g/cm^2. This is rather close to our estimations performed for the southern province ($>70\,°S$) assuming a soil density of 1.4–1.6 g/cm^3 (see Figs. 3 and 4).

5. Distribution of CO$_2$ deposition at Mars polar regions

Analysis of seasonal variations of CO$_2$ deposition is based on the solution of *Task2* of the HEND data deconvolution. *Task2* may be considered when *Task1* has already been accomplished (see Section 4).
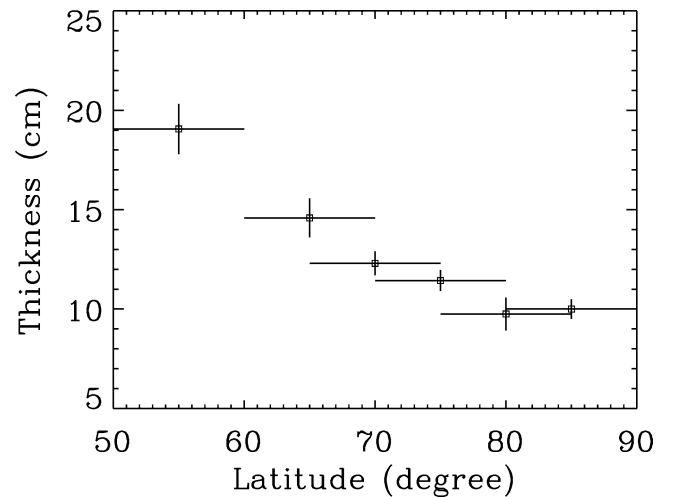
This means that the best fitting parameters, which describe the composition of the ground subsurface, can be fixed according to *Task1*. To estimate the seasonal deposition of carbon dioxide, we solve *Task2* with the column density of the CO$_2$ deposition as the variable parameter. Varying the column density, one may find the best correspondence between model predictions and experimental data by the minimizing function (2) (see Section 3 above).

For the northern hemisphere, measurements started at the end of winter, so we have observed the transition from the maximal presence of the CO$_2$ deposit to the stage of its sublimation into the martian atmosphere. In contrast, in the southern hemisphere, the initial period of observations corresponds to late summer, when the presence of CO$_2$ deposition was limited by the southern residual cap. Going farther into southern fall, we have observed how the CO$_2$ frost gets thicker as it condenses from the enormous mass of atmospheric carbon dioxide. In both cases, the observational data allow the study of the dynamics of the seasonal caps and the determination of when the accumulation of CO$_2$ reached its maximum. The last value may be used to estimate the total masses of the seasonal caps at both hemispheres.

Table 3
Southern hemisphere—parameters of double layered model

South regions coordinates (degree)				Depth (cm)	Water (%)	Probability for double layered model
Longitude1	Longitude2	Latitude1	Latitude2			
0	15	−60	−50	25.0	2.6	0.4
15	30	−60	−50	25.0	2.6	0.4
30	45	−60	−50	25.0	7.3	0.4
45	60	−60	−50	10.0	8.1	0.4
60	75	−60	−50	15.0	25.0	0.4
75	90	−60	−50	10.0	12.6	0.6
90	105	−60	−50	10.0	15.1	0.5
105	120	−60	−50	15.0	24.5	0.3
120	135	−60	−50	20.0	25.0	0.4
135	150	−60	−50	15.0	8.1	0.6
150	165	−60	−50	25.0	11.8	0.9
165	180	−60	−50	25.0	6.9	0.6
180	195	−60	−50	10.0	3.5	0.2
195	210	−60	−50	25.0	4.5	0.3
210	225	−60	−50	20.0	3.6	0.4
225	240	−60	−50	15.0	3.2	0.5
240	255	−60	−50	20.0	2.7	0.7
255	270	−60	−50	25.0	4.4	0.7
270	285	−60	−50	20.0	3.3	0.4
285	300	−60	−50	25.0	3.5	0.8
300	315	−60	−50	7.5	2.9	0.8
315	330	−60	−50	25.0	5.1	0.8
330	345	−60	−50	25.0	6.7	0.8
345	360	−60	−50	20.0	4.0	0.4
0	15	−70	−60	20.0	25.0	0.9
15	30	−70	−60	20.0	26.6	0.6
30	45	−70	−60	10.0	12.3	0.8
45	60	−70	−60	15.0	17.7	0.4
60	75	−70	−60	7.5	21.3	0.7
75	90	−70	−60	10.0	43.2	0.3
90	105	−70	−60	10.0	42.6	0.7
105	120	−70	−60	10.0	31.8	0.5
120	135	−70	−60	10.0	31.4	0.3
135	150	−70	−60	15.0	39.9	0.9
150	165	−70	−60	15.0	32.6	0.4
165	180	−70	−60	15.0	24.0	0.5
180	195	−70	−60	10.0	15.1	0.7
195	210	−70	−60	15.0	22.1	0.2
210	225	−70	−60	10.0	14.0	0.8
225	240	−70	−60	20.0	31.8	0.8
240	255	−70	−60	20.0	28.8	0.7
255	270	−70	−60	15.0	22.1	0.4
270	285	−70	−60	15.0	25.1	0.5
285	300	−70	−60	20.0	40.2	0.4
300	315	−70	−60	20.0	54.1	0.4
315	330	−70	−60	15.0	23.7	0.9
330	345	−70	−60	7.5	9.9	0.8
345	360	−70	−60	25.0	32.5	0.8
0	18	−75	−65	15.0	40.0	0.5
18	36	−75	−65	15.0	40.0	0.6
36	54	−75	−65	15.0	39.1	0.7
54	72	−75	−65	10.3	27.7	0.1
72	90	−75	−65	8.0	45.0	0.2
90	108	−75	−65	12.0	61.0	0.4
108	126	−75	−65	13.0	54.0	0.3
126	144	−75	−65	16.0	70.0	0.2
144	162	−75	−65	12.5	49.0	0.2
162	180	−75	−65	16.5	70.0	0.2
180	198	−75	−65	16.3	70.0	0.4
198	216	−75	−65	11.5	38.0	0.2
216	234	−75	−65	10.0	26.5	0.6

Table 3 (*continued*)

South regions coordinates (degree)				Depth (cm)	Water (%)	Probability for double layered model
Longitude1	Longitude2	Latitude1	Latitude2			
234	252	−75	−65	10.0	21.2	0.7
252	270	−75	−65	10.0	28.7	0.2
270	288	−75	−65	10.0	27.8	0.4
288	306	−75	−65	10.0	32.3	0.3
306	324	−75	−65	10.0	40.0	0.1
324	342	−75	−65	10.0	25.0	0.8
342	360	−75	−65	15.0	26.5	0.6
0	24	−80	−70	12.5	52.6	0.7
24	48	−80	−70	12.5	52.8	0.7
48	72	−80	−70	12.5	62.5	0.5
72	96	−80	−70	12.5	66.2	0.5
96	120	−80	−70	12.5	65.0	0.5
120	144	−80	−70	12.5	55.0	0.1
144	168	−80	−70	12.5	66.4	0.1
168	192	−80	−70	10.0	39.5	0.3
192	216	−80	−70	12.5	68.2	0.1
216	240	−80	−70	12.5	60.1	0.4
240	264	−80	−70	12.5	65.3	0.6
264	288	−80	−70	12.5	73.8	0.5
288	312	−80	−70	8.0	36.4	0.3
312	336	−80	−70	10.0	47.0	0.1
336	360	−80	−70	6.0	25.3	0.4
0	36	−85	−75	10.0	66.3	0.4
36	72	−85	−75	10.0	48.8	0.3
72	108	−85	−75	12.5	62.4	0.3
108	144	−85	−75	12.5	64.5	0.2
144	180	−85	−75	10.0	49.3	0.2
180	216	−85	−75	8.0	36.7	0.2
216	252	−85	−75	12.5	70.0	0.3
252	288	−85	−75	10.0	68.2	0.3
288	324	−85	−75	8.0	43.8	0.1
324	360	−85	−75	4.0	31.5	0.2
0	72	−90	−80	10.0	53.1	0.5
72	144	−90	−80	10.0	64.4	0.2
144	216	−90	−80	10.0	51.3	0.1
216	288	−90	−80	10.0	64.4	0.3
288	360	−90	−80	10.0	55.0	0.2

Neutron and gamma-ray spectroscopy are able to provide independent estimations of the CO_2 deposit's mass. The total mass M of the CO_2 deposit covering the surface of a particular region may be estimated as $M = \Delta \times S \times h \equiv S \times C_d$. Where Δ is the density of the CO_2 deposit; h is the linear thickness of the CO_2 deposit, S is the surface area, and C_d is the column density of the seasonal deposit.

We estimated the column density of the deposition of CO_2 for each of 172 selected regions in the northern and southern hemispheres of Mars. Additionally, the whole period of observation was divided into a set of time intervals which cover the transition between different seasons of the martian year. There were 11 and 12 such periods selected for northern and southern hemispheres, respectively. The multidimensional modeling of the CO_2 deposition on Mars is based on the solutions of *Task2* of the HEND data analysis for 814 cases for the north (74 surface elements × 11 season periods) and for 1176 cases for the south (98 surface elements × 12 season periods).

The time history of the condensed mass of the CO_2 deposit at different northern and southern latitude belts is presented on the upper graphs of Figs. 5, 6. For both poles, there is a definite

latitude dependence of the condensation and sublimation of the CO_2 deposit in the early spring. When carbon dioxide starts to sublime from the lower latitudes, it is still stable or even is still accumulating at higher latitudes. There is a time delay of the maximal accumulation of condensed mass for higher latitudes in comparison with lower latitude belts near the borders of the seasonal caps. It is also seen that the peaks of accumulation at high latitudes are broader and smoother than the peaks observed at lower latitudes belts.

The contribution to the total CO_2 mass varies for different latitude belts. Although the polar regions are covered by the thickest layer of CO_2, they contribute a significantly smaller fraction to the total mass of the seasonal cap when compared to the lower latitude belts with a larger area.

Estimations of the annual changes of the total mass of the seasonal caps are also presented on Figs. 5, 6 (bottom graph). In addition to HEND data on these graphs, we present recent numerical simulations of the seasonal cap masses derived from the GCM (shown by dashed line, Smith and Zuber, 2003). Analysis of the HEND observations shows that the maximum condensed mass at the North may be estimated as $(3.8 \pm 0.2) \times 10^{15}$ kg (see
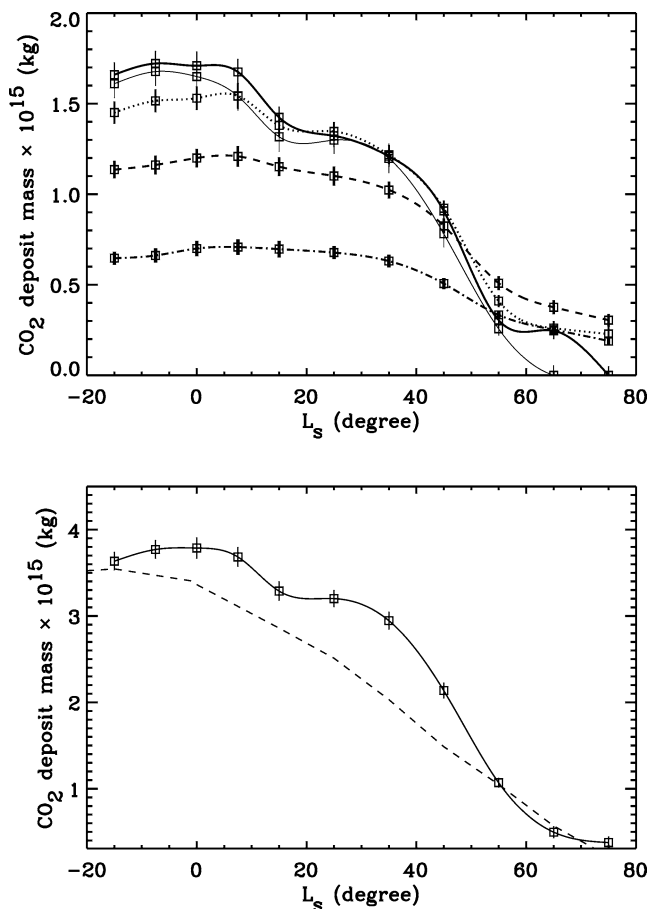
Fig. 5. Changes in the CO_2 mass of the northern seasonal cap as a function of time. Temporal behavior of the total mass of the northern seasonal cap (solid line) and GCM predictions (dashed line) are shown on the bottom graph. Curves showing changes of the CO_2 deposit mass at different northern latitudes are shown on the top graph as a function of time. The thin line corresponds to the $60\,°N$–$70\,°N$ latitude belt; the thick line corresponds to the $65\,°N$–$75\,°N$ latitude belt; the dotted line corresponds to the $70\,°N$–$80\,°N$ latitude belt, the dashed line corresponds to $75\,°N$–$85\,°N$, and the dash-dotted line corresponds to $80\,°N$–$90\,°N$.
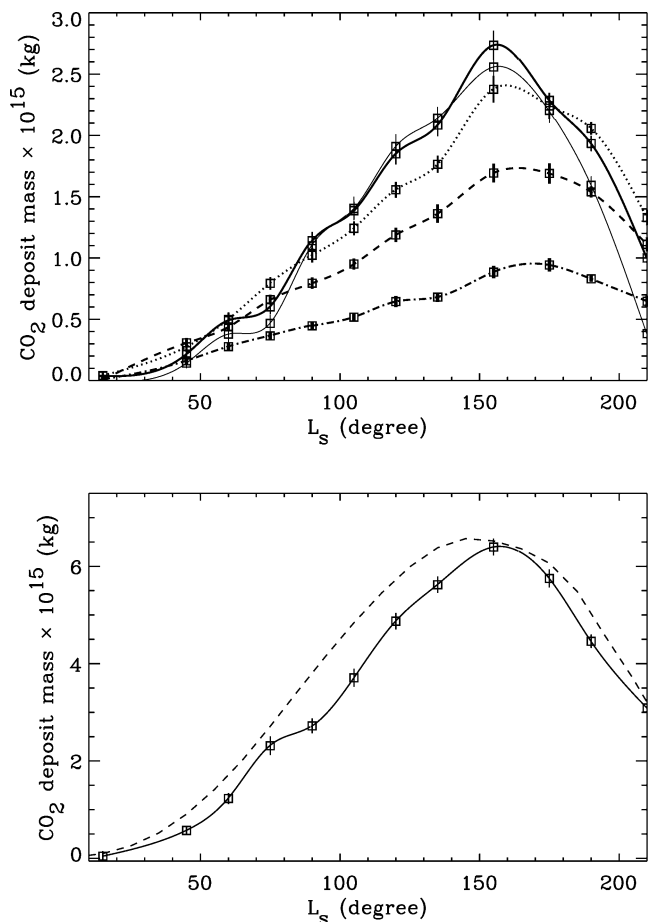

Fig. 6. Changes of the mass of the southern seasonal cap as a function of time. Temporal behavior of the total mass of the southern seasonal cap (solid line) and GCM predictions (dashed line) are shown on the bottom graph. Curves showing changes of the CO_2 deposit mass at different southern latitudes are shown on the top graph as a function of time. The thin line corresponds to the $60\,°S$–$70\,°S$ latitude belt; the thick line corresponds to the $65\,°S$–$75\,°S$ latitude belt; the dotted line corresponds to the $70\,°S$–$80\,°S$ latitude belt, the dashed line corresponds to $75\,°S$–$85\,°S$, and the dash-dotted line corresponds to $80\,°S$–$90\,°S$.

Fig. 5). It was observed at $L_s \sim 5°$ between the end of northern winter and the beginning of northern spring. This value is found to be close to the predictions of the GCM (see Fig. 5). But, it is the only case of good correspondence between the numerical simulations from the GCM and the HEND experimental measurements. According to the GCM, the maximum mass of the CO_2 deposit in the northern hemisphere has to occur significantly earlier (~ 10 degrees of L_s) than was found from analysis of the HEND data. The shapes of the GCM and HEND mass time profiles also look quite different. The largest difference between the two mass estimations may be up to 30% for particular seasonal intervals.

It is difficult to explain this effect by systematic errors in HEND data analysis. The systematic errors (if they exist) play a dominant role in the wrong estimation of CO_2 frost column density (y-axis in Figs. 5, 6), but do not significantly change the observed time history of condensation/sublimation processes (x-axis in Figs. 5, 6) because they act equally on datasets gathered at different times. Moreover, the comparison between

HEND, Mars Odyssey/NS, and the GCM estimation of CO_2 frost at polar latitudes [see NS results published in Feldman et al., (2003a, 2003b)] demonstrates quite a good correspondence between different types of data. Our data analysis shows that the time lag between the HEND and GCM estimations of the masses of the polar caps is found to be ~ 2–3 weeks. This discrepancy should mainly be attributed to the moderate latitudes.

The main conclusion that may be derived here is that neutron observations give a very similar estimation for the mass of the northern seasonal cap in comparison to numerical simulations of the martian atmosphere (see, for example, Smith and Zuber, 2003). But, the obtained variations of the condensed mass at the northern hemisphere do not correlate well. The last fact requires close attention and further data analysis to understand the nature of the phenomenon.

For the southern seasonal cap, the maximum accumulation of condensed CO_2 mass may be estimated as $(6.3 \pm 0.2) \times 10^{15}$ kg (see Fig. 6). This maximum is observed at the end of

southern winter ($L_s \sim 150°$–$160°$). Comparison between GCM numerical simulations and HEND results shows good correspondence between both time curves. The HEND mass curve less below the GCM time profile, but the difference between these curves is not as large as it was found to be for the northern hemisphere. The estimations of the maximum mass of the southern seasonal cap also provide similar values in both cases. However, the observed moment of peak mass accumulation is about 10 degree of L_s later than predicted by the GCM. This is similar to the northern hemisphere case.

Previous estimations of the mass of the CO_2 deposition were derived from predictions of the GCM as from analysis of Mars Global Surveyor (MGS) experimental data (Smith et al., 2001, 2003; Kieffer and Titus, 2001; Yoder et al., 2003). For MGS, the redistribution of CO_2 mass between the martian poles influences the spacecraft in orbit. Using precise models of the gravity potential, it is possible to convert distortions of the spacecraft orbit into the variable masses of the seasonal caps (Smith et al., 2001, 2003; Yoder et al., 2003). This approach is strictly model dependent and does not have very high accuracy. So, the estimations made by Yoder et al. (2003) correspond to the broad range from 3.7×10^{15} up to 8.6×10^{15} kg for the northern seasonal cap. The total mass of the southern seasonal cap was estimated to be 30–40% larger than for the northern cap.

The neutron and gamma-ray measurements are sensitive to the column density (g/cm^2) and cannot provide estimations of the linear thickness of the CO_2 deposition. It is necessary to know the density of the CO_2 deposit to convert column density to linear thickness measured in cm (column density = linear thickness × density). The density of the seasonal deposit can be taken from MOLA data onboard MGS for the previous martian year (Smith et al., 2001, 2003; Yoder et al., 2003). It may also be estimated from the direct comparison between the column density of CO_2 measured by neutron instruments and the CO_2 thickness variation measurements by MOLA.

Such attempts have already been done using neutron spectroscopy data gathered onboard Mars Odyssey (HEND, NS) and elevation data from MOLA/MGS (Mitrofanov et al., 2003a; Aharonson et al., 2004, in press). The quality of the MOLA measurements is very high at polar latitudes where the thickness of the CO_2 deposit is close to its maximum value. But, the measurement quality is low at the border of the seasonal cap where the thickness is too small in comparison to the MOLA resolution of about 20 cm. On other hand, the HEND measurements are not very sensitive to the thickness of the CO_2 deposition at the polar regions because the column density of the CO_2 frost is comparable to the thickness of the layer in which the neutron production occurs. After a thickness of about 1 m, a larger thickness of CO_2 does not lead to a change in neutron production. But at low latitudes, HEND has a higher efficiency than MOLA for measurements of the CO_2 layer because even several centimeters of CO_2 changes the leakage flux of neutrons enough for reliable measurements of the seasonal deposition (Litvak et al., 2003a, 2004). Taking this fact into account, one concludes that the polar latitudes (70°–85°) present the most favorable region over which to perform density es-
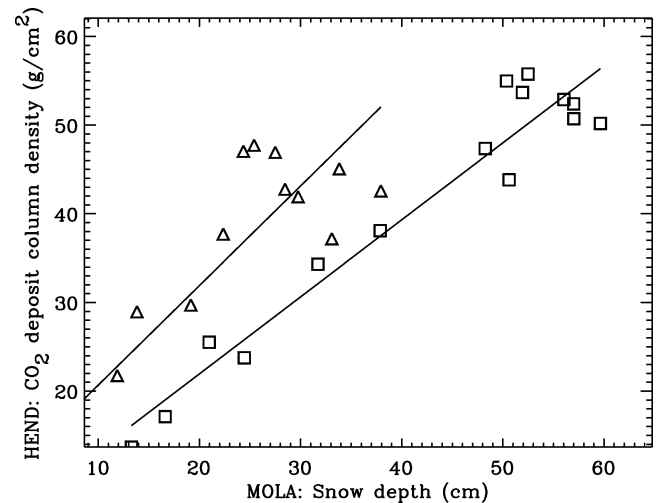

Fig. 7. Comparison between HEND CO_2 frost column density and MOLA snow depths for same martian seasons. The measurements for 75 °N–85 °N latitude belt are shown by squares and measurements for 70 °N–80 °N latitude belt are shown by triangles. The straight lines represent best fits extracted from the approximation of the data by a linear model.

timations. Using results published in Smith et al. (2001) and Mitrofanov et al. (2003a) together with current estimations of CO_2 column density at different latitudes, one may provide rough estimations of the CO_2 mass density. To explain our estimations of the CO_2 deposit density, we have included a graph (see Fig. 7) describing the dependency of the CO_2 column density (g/cm^2, HEND data) on the deposit's linear thickness (cm, MOLA data, published in Smith et al., 2001). Each data point on the graph corresponds to a particular martian season for which HEND and MOLA data are available. Here we present two northern latitude belts: 70 °N–80 °N and 75 °N–85 °N. The evident correlation between the two types of data allows us to extract the density of the CO_2 frost for a given latitude belt. The slope of a line fitting the experimental points is an estimate of the CO_2 deposit density ($\sim$0.9 g/cm^3 for 75 °N–85 °N and $\sim$1.1 g/cm^3 for 70 °N–80 °N, see Fig. 7, this technique was tested in Aharonson et al., 2004, in press). Taking into account the scattering of the experimental points, it is difficult to draw strong conclusions about the latitude dependence of the inferred CO_2 deposit density. But, these results may be an indication that such latitude-dependent density effects may be detected in further analysis.

6. Conclusions

In this paper, we have compared polar regions of Mars using neutron spectroscopy data from the HEND instrument onboard Mars Odyssey. Analysis of the neutron albedo of Mars may be considered a powerful tool for studying the distribution of water–ice in subsurface layers of the planet. Regional variations of the neutron flux observed at high northern and southern latitudes during the summer seasons are mainly produced by a non-homogeneous surface distribution of water–ice. Temporal variations of the neutron flux as a function of the martian seasons result from the time-dependent nature of the deposition of

atmospheric CO_2. These data can be converted into estimations of the masses of the CO_2 deposits that seasonally condense at the polar regions.

To deconvolve measurements of neutron flux into estimations of water content, it is necessary to assume a model for the martian regolith. Here, we have tested the two simplest models: a depth-homogeneous model and a double-layered model. It was found that the homogeneous model provides appropriate agreement with observations for the northern polar region. Data analysis shows that dirty water–ice is placed very close to the surface at high northern latitudes. It may be covered by a very thin layer of dust with a thickness of at most a few centimeters. The distribution of water–ice is latitude dependent: the mass fraction of water increases from 10–15% at 60 °N to ~50% at more poleward latitudes.

For the south polar region, we also found approximately the same mass fraction of water as in the northern hemisphere. But, the data gathered for the southern hemisphere disagree with the homogeneous model. It was shown that the double-layered model of the regolith works well: the water–ice rich layers are covered by a dry layer of soil with a thickness of about 10–20 cm.

Taking into account that northern permafrost ice is located close to the surface, we think that one may assume it actively interacts with the martian atmosphere. It leads to speculations that at the present epoch, the formation of the northern ice shield is still in progress. In the southern hemisphere, the interactions between the martian atmosphere and water–ice are severely diminished by the top layer of dry soil. It may point out that the formation process of the water–ice shield was finished in the southern hemisphere a long time ago as a dry layer was formed.

We also analyzed temporal variations of neutron flux at polar regions. These variations are controlled by the global redistribution of atmospheric CO_2 between the martian poles. From analysis of seasonal changes of neutron flux, we have derived the time curves of the mass variations within the northern and southern seasonal caps. It was found that the maximum mass of the southern seasonal cap can be estimated as $(6.3 \pm 0.2) \times 10^{15}$ kg, which is 40–50% larger than the mass of the northern seasonal cap [$(3.8 \pm 0.2) \times 10^{15}$ kg]. These results are in good agreement with calculations based on the GCM. But, according to observations of neutron flux, the accumulation of the maximum condensed mass occurred ~10 degrees of L_s later than what follows from GCM predictions (Smith and Zuber, 2003).

There are definite possibilities for further development of the methods described in this paper. The next step in this direction concerns comparing different types of experimental data. The first preliminary analysis of gamma-ray and neutron data shows that the distribution of water–ice throughout the subsurface in the south polar region may be more complicated than can be adequately described by a double-layered model (Boynton et al., 2003a, 2003b). To effectively utilize the combination of both types of data, one ought to consider models with a multilayered structure for such analysis (Boynton et al., 2003a, 2003b). Unfortunately, the realization of this approach is very laborious. It requires a significantly larger number of parameters and enormous time for calculation and verification.

References

Aharonson, O., Zuber, M.T., Smith, D.E., Neumann, G.A., Feldman, W.C., Prettyman, T.H., 2004. Depth, distribution, and density of CO_2 deposition on Mars. J. Geophys. Res. 109, doi:10.1029/2003JE002223. E05004.

Boynton, W.V., Feldman, W.C., Squyres, S.W., Prettyman, T.H., Brückner, J., Evans, L.G., Reedy, R.C., Starr, R., Arnold, J.R., Drake, D.M., Englert, P.A., Metzger, A.E., Mitrofanov, I.G., Trombka, J.I., d'Uston, C., Wanke, H., Gasnault, O., Hamara, D.K., Janes, D.M., Marsialis, R.L., Maurice, S., Mikheeva, I., Taylor, G.J., Tokar, R., Shinohara, C., 2002. Distribution of hydrogen in the near surface of Mars: Evidence for subsurface ice deposits. Science 297, 81–85.

Boynton, W.V., Chamberlain, M., Feldman, W.C., Prettyman, T., Hamara, D., Janes, D., Kerry, K., 2003a. Abundance and distribution of ice in the polar regions of Mars: More evidence for wet periods in the recent past. Sixth International Conference on Mars, California. Abstract #3259.

Boynton, W.V., Chamberlain, M., Feldman, W.C., Prettyman, T., Hamara, D., Janes, D., Kerry, K., 2003b. Ice in the polar regions of Mars: Evidence for wet periods in the recent past. 3rd International Conference on Mars Polar Science. Abstract #8133.

Boynton, W.V., Feldman, W.C., Mitrofanov, I.G., Evans, L.G., Reedy, R.C., Squyres, S.W., Starr, R., Trombka, J.I., d'Uston, C., Arnold, J.R., Englert, P.A.J., Metzger, A.E., Wanke, H., Bruckner, J., Drake, D.M., Shinohara, C., Fellows, C., Hamara, D.K., Harshman, K., Kerry, K., Turner, C., Ward, M., Barthe, H., Fuller, K.R., Storms, S.A., Thornton, G.W., Longmire, J.L., Litvak, M.L., Ton'chev, A.K., 2004. The Mars Odyssey Gamma-Ray Spectrometer instrument suite. Space Sci. Rev. 110 (1), 37–83.

Drake, D.M., Feldman, W.C., Jakosky, B.M., 1988. Martian neutron leakage spectra. J. Geophys. Res. 93, 6353–6368.

Feldman, W.C., Boynton, W.V., Jakosky, B.M., Mellon, M.T., 1993. Redistribution of subsurface neutrons caused by ground ice on Mars. J. Geophys. Res. 98, 20855–20870.

Feldman, W.C., Boynton, W.V., Tokar, R.L., Prettyman, T.H., Gasnault, O., Squyres, S.W., Elphic, R.C., Lawrence, D.J., Lawson, S.L., Maurice, S., McKinney, G.W., Moore, K.R., Reedy, R.C., 2002. Global distribution of neutrons from Mars: Results from Mars Odyssey. Science 297, 75–78.

Feldman, W.C., Prettyman, T.H., Boynton, W.V., Murphy, J.R., Squares, S., Maurice, S., Tokar, R.L., McKinney, G.W., Hamara, D.K., Kelly, N., Kerry, K., 2003a. CO_2 frost cap thickness on Mars during northern winter and spring. J. Geophys. Res., doi:10.1029/2003JE002101.

Feldman, W.C., Prettyman, T.H., Boynton, W.V., Squyres, S.W., Bish, D.L., Elphic, R.C., Funsten, H.O., Lawrnce, D.J., Maurice, S., Moore, K.R., Tokar, R.L., Vaniman, D.T., 2003b. The global distribution of near-surface hydrogen on Mars. Sixth International Conference on Mars. Abstract #3218.

Feldman, W.C., Prettyman, T.H., Maurice, S., Plaut, J.J., Bish, D.L., Vaniman, D.T., Mellon, M.T., Metzger, A.E., Squyres, S.W., Karunatillake, S., Boynton, W.V., Elphic, R.C., Funsten, H.O., Lawrence, D.J., Tokar, R.L., 2004. Global distribution of near-surface hydrogen on Mars. J. Geophys. Res. 109, doi:10.1029/2003JE002160. E09006.

Foley, C.N., Economou, T.E., Clayton, R.N., Dietrich, W., 2003a. Calibration of the Mars Pathfinder alpha proton X-ray spectrometer. J. Geophys. Res., doi:10.1029/2002JE002018.

Foley, C.N., Economou, T., Clayton, R.N., 2003b. Final chemical results from the Mars Pathfinder alpha proton X-ray spectrometer. J. Geophys. Res., doi:10.1029/2002JE002019.

Forget, F., Pollack, J., 1996. Thermal infrared observations of the condensing martian polar caps: CO_2 ice temperatures and radiative budget. J. Geophys. Res. 101, 16865–16879.

Haberle, R.M., Pollack, J.B., Barnes, J.R., Zurek, R.W., Leovy, C.B., Murphy, J.R., Lee, H., Schaeffer, J., 1993. Mars atmospheric dynamics as simulated by the NASA AMES General Circulation Model. I. The zonal-mean circulation. J. Geophys. Res. 98, 3093–3123.

Haberle, R.M., Murphy, J.R., Schaeffer, J., 2003. Orbital change experiments with a Mars general circulation model. Icarus 161, 66–89.

Head, J.W., Mustard, J.F., Kreslavsky, M.A., Mililen, R.E., Marchant, D.R., 2003. Recent ice ages on Mars. Nature 426, 797–802.

Kieffer, H.H., 1979. Mars south polar spring and summer temperatures—A residual CO_2 frost. J. Geophys. Res. 84, 8263–8288.

Kieffer, H.H., Titus, T.N., 2001. TES mapping of Mars' north seasonal cap. Icarus 154, 162–180.

Laskar, J., Robutel, P., 1993. The chaotic obliquity of the planets. Nature 362, 608–612.

Laskar, J., Levrard, B., Mustard, J.F., 2002. Orbital forcing of the martian polar layered deposits. Nature 419, 375–377.

Leighton, R.B., Murray, B.C., 1966. Behavior of carbon dioxide and other volatiles on Mars. Science 153, 136–144.

Litvak, M.L., Mitrofanov, I.G., Kozyrev, A.S., Sanin, A.B., Tretyakov, V., Smith, D.E., Zuber, M.T., Boynton, W.V., Hamara, D.K., Shinohara, C., Saunders, R.S., Drake, D., 2003a. 4-D model of CO_2 deposition at north and south of Mars from HEND/Odyssey and MOLA/MGS. Sixth International Conference on Mars, California. Abstract #3040.

Litvak, M.L., Mitrofanov, I.G., Kozyrev, A.S., Sanin, A.B., Tret'yakov, V.I., Boynton, W.V., Shinohara, C., Hamara, D., Saunders, S., Drake, D.M., Zuber, M.T., Smith, D.E., 2003b. Seasonal neutron-flux variations in the polar caps of Mars as revealed by the Russian HEND instrument onboard the NASA 2001 Mars Odyssey Spacecraft. Solar Syst. Res. 37, 378–386.

Litvak, M.L., Mitrofanov, I.G., Kozyrev, A.S., Sanin, A.B., Tret'yakov, V.I., Boynton, W.V., Shinohara, C., Hamara, D., Saunders, S., Drake, D.M., Zuber, M.T., Smith, D.E., 2004. Seasonal carbon dioxide depositions on the martian surface as revealed from neutron measurements by the HEND instrument onboard the 2001 Mars Odyssey Spacecraft. Solar Syst. Res. 38 (3), 167–177.

Masarik, J., Reedy, R.C., 1996. Gamma ray production and transport in Mars. J. Geophys. Res. 101, 18891–18912.

Mellon, M.T., Jakosky, B.M., 1995. The distribution and behavior of martian ground ice during past and present epochs. J. Geophys. Res. 100, 11781–11799.

Mellon, M.T., 2003. Theory of ground ice on Mars and the implications to the neutron leakage flux. Lunar Planet. Sci. XXXIV. Abstract #1916.

Mellon, M.T., Feldman, W.C., Prettyman, T.H., 2004. The presence and stability of ground ice in the southern hemisphere of Mars. Icarus 169, 324–340.

Mischna, M.A., Richardson, M.I., Wilson, R.J., McCleese, D.J., 2003. On the orbital forcing of martian water and CO_2 cycles: A general circulation model study with simplified volatile schemes. J. Geophys. Res. 108, doi:10.1029/2003JE002051.

Mitrofanov, I.G., Anfimov, D., Kozyrev, A., Litvak, M., Sanin, A., Tret'yakov, V., Krylov, A., Shvetsov, V., Boynton, W., Shinohara, C., Hamara, D., Saunders, R.S., 2002. Maps of subsurface hydrogen from the High Energy Neutron Detector, Mars Odyssey. Science 297, 78–81.

Mitrofanov, I.G., Zuber, M.T., Litvak, M.L., Boynton, W.V., Smith, D.E., Drake, D., Hamara, D., Kozyrev, A.S., Sanin, A.B., Shinohara, C., Saunders, R.S., Tretyakov, V., 2003a. CO_2 snow depth and subsurface water–ice abundance in the northern hemisphere of Mars. Science 300, 2081–2084.

Mitrofanov, I.G., Litvak, M.L., Kozyrev, A.S., Sanin, A.B., Tret'yakov, V.I., Boynton, W.V., Shinohara, C., Hamara, D., Saunders, S., Drake, D.M.,

2003b. Search for water in martian soil using global neutron mapping by the Russian HEND instrument onboard the US 2001 Mars Odyssey Spacecraft. Solar Syst. Res. 37, 366–377.

Mitrofanov, I.G., Litvak, M.L., Kozyrev, A.S., Sanin, A.B., Tret'yakov, V.I., Boynton, W.V., Shinohara, C., Hamara, D., Saunders, 2004a. Estimation of water content in martian regolith from neutron measurements by HEND onboard 2001 Mars Odyssey. Solar Syst. Res. 38 (4), 253–257.

Mitrofanov, I.G., 2004b. Global distribution of subsurface water. In: Tokano, T. (Ed.), Water on Mars and Life. ISBN 3-540-20624-8. Springer, Berlin. Chapter V.

Prettyman, T.H., Feldman, W.C., Boynton, W.V., McKinney, G.W., Lawrence, D.J., Mellon, M.T., 2003. Atmospheric corrections for neutrons reveal variations in surface composition in the Tharsis region. Lunar Planet. Sci. XXXIV. Abstract #1950.

Prettyman, T.H., Feldman, W.C., Mellon, M.T., McKinney, G.W., Boynton, W.V., Karunatillake, S., Lawrence, D.J., Maurice, S., Metzger, A.E., Murphy, J.R., Squyres, S.W., Starr, R.D., Tokar, R.L., 2004. Composition and structure of the martian surface at high southern latitudes from neutron spectroscopy. J. Geophys. Res. 109, doi:10.1029/2003JE002139.

Reedy, R.C., 1987. Nuclide production by primary cosmic-ray protons. J. Geophys. Res. 92 (B4), E697–E702.

Richardson, M.I., Wilson, R.J., 2002. Investigation of the nature and stability of the martian seasonal water cycle with a general circulation model. J. Geophys. Res. 107, doi:10.1029/2001JE001536.

Richardson, M.I., McCleese, D.J., Mischna, M., Vasavada, A.R., 2003. Obliquity, ice sheets, and layered sediments on Mars: What spacecraft observations and climate models are telling us. Lunar Planet. Sci. XXXIV. Abstract #1281.

Smith, D.E., Zuber, M.T., Neumann, G.A., 2001. Seasonal variations of snow depth on Mars. Science 294, 2141–2146.

Smith, D.E., Zuber, M.T., 2003. The masses of Mars's seasonal polar icecaps. 3rd International Conference on Mars Polar Science. Abstract #8063.

Tokar, R.L., Feldman, W.C., Prettyman, T.H., Moore, K.R., Lawrence, D.J., Elphic, R.C., Kreslavsky, M.A., Head, J.W., Mustard, J.F., Boynton, W.V., 2002. Ice concentration and distribution near the south pole of Mars: Synthesis of odyssey and global surveyor analyses. Geophys. Res. Lett. 29, doi:10.1029/2002GL015691, 1904.

Tokar, R.L., Elphic, R.C., Feldman, W.C., Funsten, H.O., Moore, K.R., Prettyman, T.H., Wiens, R.C., 2003. Mars odyssey neutron sensing of the south residual polar cap. Geoph. Res. Lett. 30 (13), doi:10.1029/2003GL017316. 10-1, CiteID 1677.

Touma, J., Wisdom, J., 1993. The chaotic obliquity of Mars. Science 259, 1294–1297.

Wänke, H., Brückner, J., Dreibus, G., Rieder, R., Ryabchikov, I., 2001. Chemical composition of rocks and soils at the pathfinder site. Space Sci. Rev. 96, 317–330.

Waters, L.S., 1999. MCNPX User's Guide (document LA-UR-99-6058). Los Alamos National Laboratory.

Yoder, C.F., Konopliv, A.S., Yuan, D.N., Standish, E.M., Folkner, W.M., 2003. Fluid core size of Mars from detection of the solar tide. Science 300, 299–303.